Article:
Liu, Y orcid.org/0000-0002-9367-3532, Song, C, Lv, G et al. (2 more authors) (2021) Evaluation of the oxidative reactivity and electrical properties of soot particles. Carbon, 178. pp. 37-47. ISSN 0008-6223

https://doi.org/10.1016/j.carbon.2021.02.086

Evaluation of the oxidative reactivity and electrical properties of soot particles

Ye Liu [a,b], Chonglin Song [a*], Gang Lv [a], Wei Zhang [a], Haibo Chen [b]

[a] State Key Laboratory of Engines, Tianjin University, Tianjin 300072, China

[b] Institute for Transport Studies, University of Leeds, Leeds LS2 9JT, UK

Abstract: This paper focuses on the correlation between the oxidative reactivity and electrical properties of soot particles. Soot particles were produced from an *n*-heptane inverse diffusion flame and were sampled at different heights above the burner (HAB) using a thermophoretic and probe sampling techniques. The electrical properties were characterized by the electrical conductivity and work function, which were evaluated by an atomic force microscopy. The soot reactivity was assessed in terms of activation energy (E_a) and characteristic oxidation temperatures, including peak temperature (T_P) and burnout temperature (T_b), using thermogravimetric analysis. As the soot particles gradually age, they have various electrical conductivity distributions. The average electrical conductivity presents an increase by three orders of magnitude when increasing the HAB from 10 to 60 mm. The work function of bulk soot particles shows an increase with the soot maturation. The soot reactivity gradually reduces during the soot maturation process because the values of E_a, T_P, and T_b show increases with the increase in HAB. For the soot particles, the E_a and T_p have strongly positive correlations with the work function and with the logarithm of the electrical conductivity. Thus, electrical properties can serve as an indicator of soot reactivity.

* Corresponding author. Tel.: +86-22-27406840-8020; fax: +86-22-27403750
Email address: songchonglin@tju.edu.cn (C.-L. Song)

Keywords: Soot particle; Electrical conductivity; Work function; Oxidative reactivity

1. Introduction

Much attention has been paid to a better understanding of the electrical properties of soot particles due to their applications in many technical fields [1-3]. The term “electrical properties” used here represents the electrical conductivity and work function. As for the application of carbon materials, electrical conductivity is a crucial intrinsic property of a material, reflecting its ability to carry a current [3-5]. Marinho et al. [6] pointed out that the discovery of high conductivity for carbon nanotubes and graphene has incredibly broadened the range of potential applications of this class of materials. Chen et al. [7] proposed that the high electrical conductivity of graphene is an important reason to become a competitive electrode material for supercapacitor applications. The work function is a parameter determining how strongly the electrons are bound in the solid and is one of the fundamental physical quantities determined the electronic structure, which significantly affects the application of carbonaceous materials as electronic devices [8-10]. Moreover, the work function is a very sensitive parameter that can provide evidence for micro- and nano-structural and chemical variations [11].

The electrical properties are strongly dependent on the nanostructure of soot particles. In our previous studies, the crystallite width was found to have a positive correlation with electrical properties for soot samples, and the interlayer distance exhibited a close negative relationship with the electrical properties [12]. Grob et al. [13] revealed that a loss of the crystalline order led to an increasing amorphization in soot, which caused a decrease in electrical conductivity. De Falco et al. [14] demonstrated that the flame-formed soot nanoparticles exhibited various electrical properties, which was intimately dependent on their nanostructure. In addition, it is widely accepted that the oxidative reactivity of soot particles is

primarily governed by soot nanostructure [15-17]. Jaramillo et al. [18] probed the oxidation kinetics and nanostructure of three model carbons and found that soot nanostructure was closely related to oxidative reactivity. Yehliu et al. [19] studied the soot particles generated from direct injection light-duty diesel engine, and the obtained results showed an excellent relationship between soot nanostructure and reactivity. At present, there have been many reports on soot nanostructure and oxidative reactivity, but studies on the correlation between soot electrical properties and oxidative reactivity are limited in number.

A better understanding of this relationship is useful to develop a method that can quickly and conveniently measure soot reactivity, which is of importance in a variety of engineering applications, such as the control of diesel soot emissions. Nowadays, diesel particulate filters (DPFs) are one of the most common technologies used for diesel soot emission control. During diesel engine operation, however, the soot particles trapped on DPFs must be periodically removed by the enhanced soot oxidation in case they clog the DPFs [20,21]. The removal of the trapped soot particles is usually implemented by an in-cylinder post-injection or a fuel injection directly into the exhaust, which can generate a large amount of total hydrocarbon (THC) emissions. These THC emissions will be oxidized by the diesel oxidation catalyst downstream, significantly raising the exhaust temperature and thus enhancing the reaction rate of soot oxidation [22]. If the changes in electrical properties can be monitored by on-board diagnostics and can reflect the real-time oxidative reactivity of soot particles in DPFs, there will be the potential of optimizing the control strategy of DPFs to achieve soot removal with less fuel consumption. For example, the soot with high reactivity is more readily oxidized, and thus less fuel is required for the increase in the exhaust temperature. In this context, the purpose

of the present work is to probe the correlation between electrical properties and oxidative reactivity of soot particles.

2. Experimental

2.1. Burner and sampling system

The schematic diagram of the experimental setup is presented in Fig. 1. An inverse diffusion flame was produced using a center-tube McKenna burner (Holthuis & Associates, U.S.A.). There are three concentric parts in the burner, which are distributed as follows: (1) a center tube with a diameter of 12.7 mm was used for supplying the mixture of oxygen and nitrogen; (2) an annular porous plug with a diameter of 30 mm for providing the *n*-heptane as fuel and Ar as a carrier gas; and (3) an outer porous plug with a diameter of 75 mm for supplying nitrogen to shield the flame from atmosphere air. The whole burner system was mounted on a lifting platform with a positional accuracy of ±0.02 mm to accurately adjust the sampling height above the burner (HAB). The *n*-heptane with high-performance liquid chromatography (HPLC) grade as fuel and Ar as a carrier gas feed a W-102A Bronkhorst vapor system to form an evaporation mixture, and at the same time, the temperature of the transmission tubes was maintained at 473 K. In parallel, a coil heater was employed to heat all the other gases up to 423 K to prevent liquid fuel condensation in the burner. The flow rates of the *n*-heptane as fuel and Ar as carrier gas were 70 g/h with an accuracy of ±0.02% and 0.31 L/min with an accuracy of ±0.2%, respectively, which was set by Bronkhorst controllers. Three independent mass flow controllers were used to set the oxygen flow rate (0.52 L/min), nitrogen flow rate (0.6 L/min), and shielding nitrogen flow rate (55 L/min). The visible flame height was 60 mm under the current operating condition, as shown in Fig. 2. Further details on the diffusion flame burner

105 system are reported in our previous study [12].

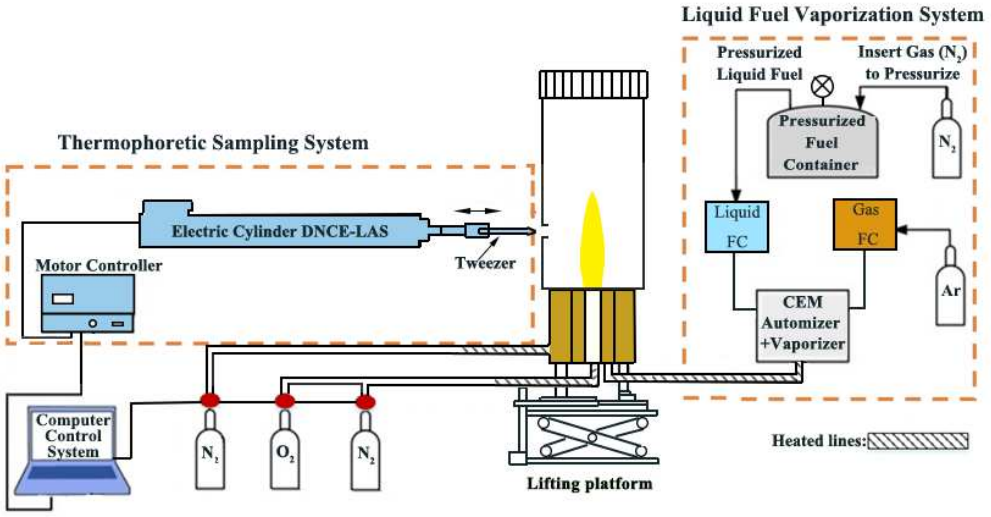

106

107 Fig. 1. Schematic diagram of the experimental setup.

108

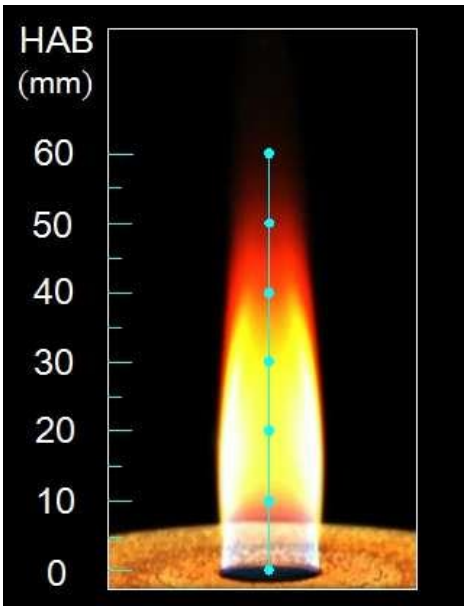

109

110 Fig. 2. An image of the experimental flame

111 A thermophoretic sampling technique based on the thermophoresis principle was
112 employed to quickly obtain the soot particles at varying HABs for the analysis of atomic force
113 microscopy (AFM). In the thermophoretic sampling technique, an advanced linear electric
114 cylinder (FESTO, Germany) was incorporated to allow for rapid and precise reciprocating
115 motion, with acceleration and speed of 120 m/s^2 and 3 m/s, and the corresponding residence

time of obtaining soot particles was 30 ms. The self-closing tweezer (N5, Switzerland) was mounted on the piston rod to fix and detach the substrate conveniently. A commercial highly oriented pyrolytic graphite (HOPG, ZYH grade, SUA) and a gold substrate were employed to load the soot samples at various HABs. A probe sampling technique shown in Fig. S1 of supplemental material was used to gain more soot samples for thermogravimetric analysis (TGA). The sampling probe with a diameter of 3.175 mm and a wall thickness of 0.125 mm was positioned horizontally over the burner. A sampling orifice with a diameter of 0.15 mm was drilled in the middle of the probe using a laser, which faced downward toward the incoming burning gas. This probe was connected to a vacuum system with an in-line Teflon filter to collect the soot particles. According to the proposed method by Zhao et al. [23], the flow rate of the dilution nitrogen and the dilution ratio was set at 29.6 L/min and 300, respectively, to quench the chemical reactions of the flame gas sucked in the sampling line. To avoid clogging the sampling orifice, each sampling time was set to one minute, and the sampling orifice was cleaned after each sampling. The sampling procedure was repeated at least five times at each sampling position to obtain sufficient soot for TGA test. To evaluate the impact of the sampling methods on soot feature, the soot particles were analyzed using X-ray diffraction (XRD). It was found that the soot particles obtained through the thermophoretic sampling method exhibited quite similar XRD patterns to those obtained through the probe sampling method (see Fig. S2 of supplemental material). This result demonstrated that the soot sampling methods had a negligible effect on the soot structure.

2.2. AFM

2.2.1. PF-TUNA

A Dimension Icon AFM (Bruker, USA) was used in this study, and the electrical conductivity of primary soot particles was determined using the PeakForce tunneling module of AFM (PF-TUNA). A Ti/Pt-coated tip (PF-TUNA probes) was selected with resonance frequency 70 kHz and spring constant 2 N/m. The HOPG with high conductivity feature was used as a substrate due to the limited influence on the electrical conductivity of soot particles [24,25]. The measurements were carried out with a calibrated optical sensitivity, and the accurate spring constant was evaluated using the thermal tune option. The *I–V* curves were obtained from the point and shoot feature of AFM at the particles in the topographical image. The typical *I–V* curve for the chosen primary soot particle is shown in Fig. 3. The calculation of the electrical conductivity (σ) is according to the following equation [14]:

$$\sigma = G\frac{4H}{\pi D^2} \tag{1}$$

where G is the electrical conductance that was obtained based on the slope of the *I–V* curves [14]. H and D are the particle height and particle bottom diameter, respectively, which were gained from the topographical images [26]. To gain statistical results, the number of selected primary soot particles was more than 150 for each soot sample, and the measure procedure for each primary soot particle was repeated at least three times to guarantee reproducibility. Here, the primary soot particles include the individual soot particles and the spherules in a soot aggregate. During measurement, the individual soot particles were chosen preferentially to avoid the mutual interference among soot particles.

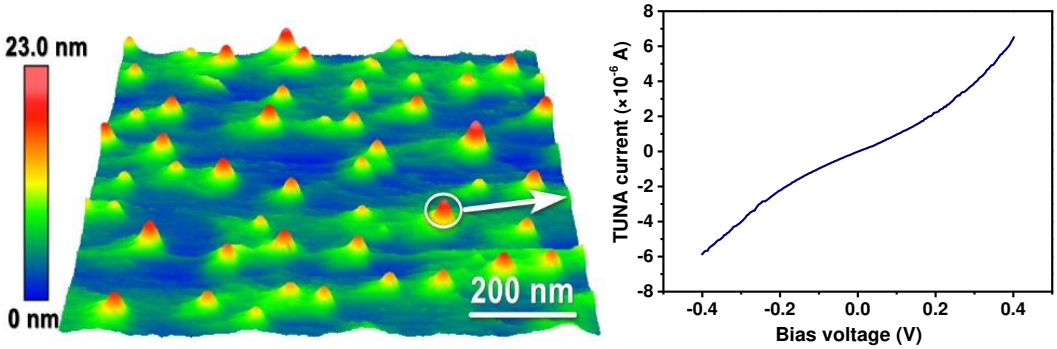

Fig. 3. Representative AFM image and *I*−*V* curve for chosen soot particle (HAB = 30 mm).

2.2.2. KPFM

The Kelvin-probe module of AFM (KPFM) was used to measure the surface potential between the probe tip of AFM and the soot sample, and the work function of the soot sample was calculated using the following equation [27]:

$$\Phi_{\text{sample}} = \Phi_{\text{tip}} - \Delta\Phi_{\text{(tip-sample)}} \quad (2)$$

where Φ_{sample} and $\Delta\Phi_{\text{tip-sample}}$ are the work function of soot sample and the surface potential between the probe tip of AFM and the soot sample, respectively. Φ_{tip} is the work function of the probe tip of AFM. A Co/Cr-coated tip was used for the measurement of soot samples, and the work function of the tip is 4.75 ± 0.03, which was provided by the AFM manufacturer. A gold substrate was used to harvest the soot particles. To avoid the effect of the gold substrate on measured results, the gold substrate was inserted into the diffusion flame many times to make sure that it was fully covered by soot particles. In addition, a gold substrate was employed to calibrate the reliability of this method. The work function of the gold substrate was calculated to be 4.93 ± 0.02 eV, in good agreement with the previous results of 4.8–5.2 eV [28,29]. All the measurements were performed in a glovebox with lower humidity to clear up the possible influence of water film on soot particles. More information on the KPFM measurement is

175 available in [12,27].

176 *2.3. TGA*

177 A thermogravimetric analyzer (Mettler-Toledo TGA/DSC1) was used to evaluate the
178 characteristic oxidation temperatures of soot samples. For each experiment, 3–4 mg of soot
179 sample was placed in a platinum crucible, and was first heated to 500 ºC and kept for 60 minutes
180 to drive off volatile compounds under ultrahigh-purity nitrogen with a flow rate of 60 ml/min.
181 After thermal treatment, the sample was cooled to 200 ºC and then was heated in ultrahigh-
182 purity air at a flow rate of 60 ml/min from 200 ºC to 800 ºC at a heating rate of 5 ºC/min. Each
183 analysis was repeated at least three times to ensure reproducibility.

184 *2.4. HRTEM*

185 The nanostructure images were obtained by means of high-resolution transmission
186 electron microscope (HRTEM) (JEOL EM-2010F) instrument with a point resolution of 0.248
187 nm operating at 200 kV. Soot samples were collected on a lacey C/Cu grid through a
188 thermophoretic sampling technique. All images were taken in a Gatan Digital Micrograph with
189 a slow-scan CCD camera (image size 2048 × 2048 pixels).

190 *2.5. XPS*

191 The oxygen functional groups and chemical composition were assessed by X-ray
192 photoelectron spectroscopy (XPS). XPS spectra were recorded on a PerkinElmer PHI-1600
193 ESCA spectrometer using an Mg Ka X-ray source. Atomic composition was calculated based
194 upon the spectra with Shirley background from survey scans. High-resolution C1s peak was
195 proceeded using commercial software CASA XPS to identify oxygenated functional groups

and carbon chemical state on soot surfaces. More detailed information on XPS has been described in the literature [12,30].

3. Results and discussion

3.1. Electrical properties

3.1.1. Electrical conductivity

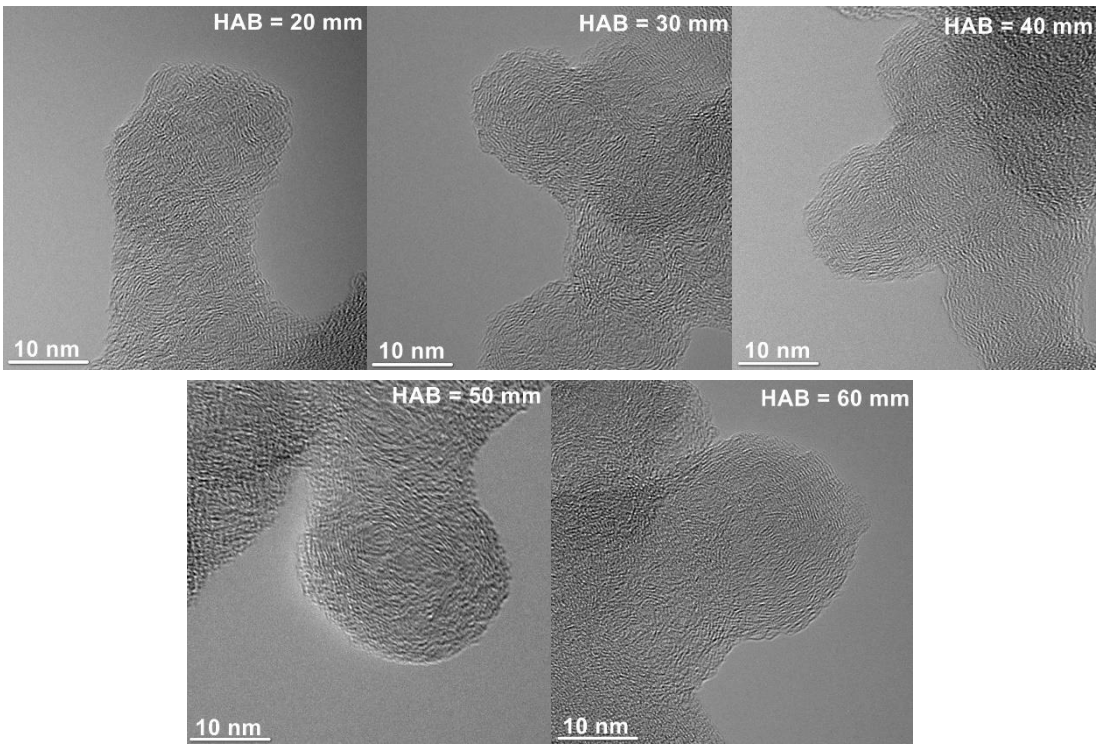

Fig. 4. HRTEM images for soot particles at various HABs

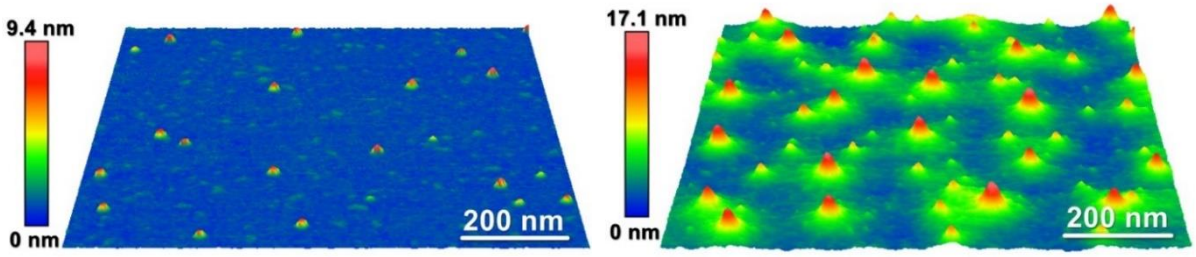

HAB = 10 mm **HAB = 20 mm**

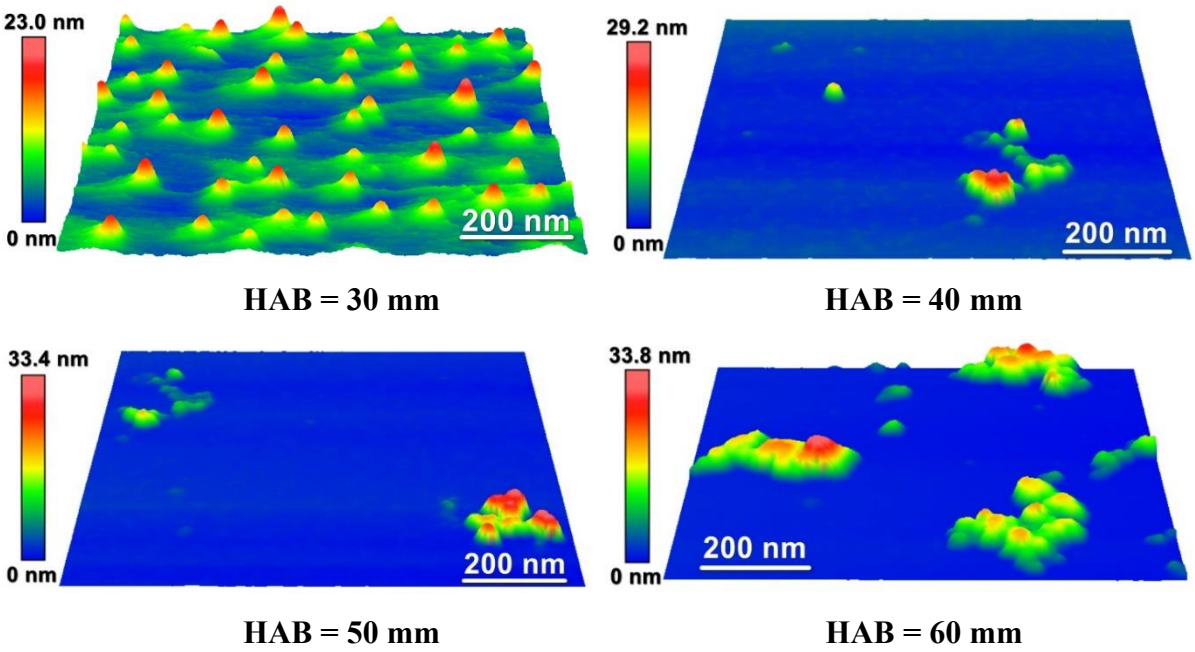

Fig. 5. AFM topographical images for soot particles at various HABs.

Previous study observed the diamond, graphitic, fullerenic and amorphous particles in a candle flame [31]. In our current flame, the soot particles exhibit graphitic and amorphous structures, and most of the soot particles have the typical shell-core nanostructure, as shown in Fig. 4. The AFM topographical images of soot particles at various HABs are shown in Fig. 5. At each HAB, more than 150 primary soot particles in the AFM topographical images were chosen for the measurement of electrical conductivity. The obtained distributions of electrical conductivity are shown in Fig. 6. The bin widths in the histograms are variable due to the significant difference in the distribution range at various HABs. It is evident that the electrical conductivity of soot particles increases with increasing the HAB. For example, the values of electrical conductivity distribute in the range of 0.03 – 0.37 S/cm at HAB= 10 mm, while they are in the range of 4.24 – 945.36 S/cm at HAB = 60 mm. The high electrical conductivity suggests that the charges can move easily inside the soot particles. To evaluate the effect of soot particle size on the electrical conductivity, more than 150 primary soot particles at HAB

= 40 mm were measured in terms of size and electrical conductivity. The mean values of electrical conductivity for the soot particles in the sizes of 14-16, 17-19, 20-22 nm are 177.63, 253.18, and 208.65 S/cm, respectively. These results suggest no definite correlation between electrical conductivity and size.

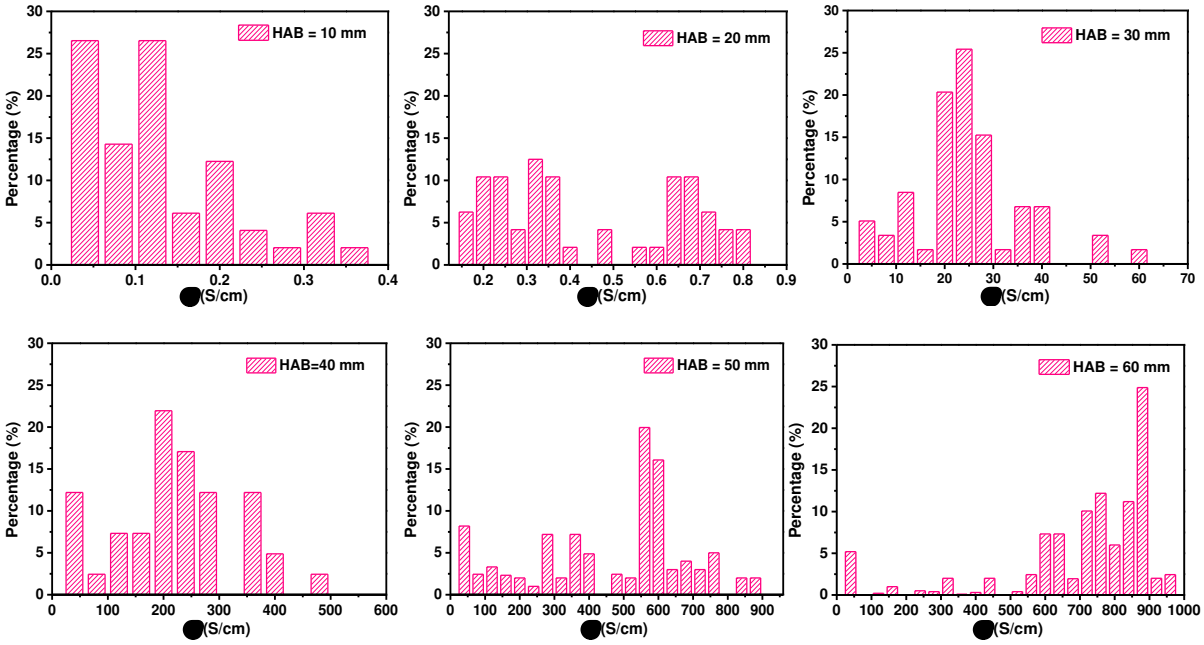

Fig. 6. Distributions of the electrical conductivity (σ) for the soot particles generated at various HABs.

To characterize such an increase in electrical conductivity quantitatively, the values of electrical conductivity at each HAB were averaged, and the obtained data were shown in Fig. 7. The averaged electrical conductivity rises sharply from 0.11 to 986.45 S/cm when increasing the HAB, and the value at HAB=10 mm is approximately three orders of magnitude lower than that at HAB=60 mm. This phenomenon can be accounted for by the soot nanostructure. As the HAB increases, the soot particles age gradually. At the same time, the graphene layers size (L_a), sp^2/sp^3 ratio and π–π stack increase and the interplanar spacing reduces (d_{002}), as illustrated in Table 1. These results imply soot development towards to more ordered nanostructure. The more ordered nanostructure is much easier for electrons jumping from one

carbon cluster to adjacent clusters and forms more delocalized π electron systems [32], and thereby the soot particles present high electrical conductivity. Grob et al. [13] measured the electrical conductivity of different carbon blacks with an increase in temperature, and found that the electrical conductivity increased sharply with the growth of crystalline carbon nanoclusters. De Falco et al. [14] investigated the electrical conductivity of bulk soot particles generated in a premixed ethylene flame, but the reported values of electrical conductivity are lower than our results. Such a phenomenon is mainly due to the differences in the synthesis conditions and parent fuels used in the studies, which result in the soot particles with different nanostructure and thus affect the electrical conductivity.

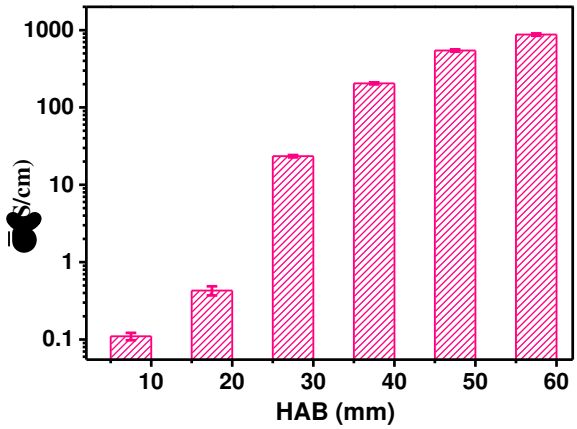

Fig. 7. Mean electrical conductivity ($\overline{\sigma}$) as functions of HABs.

Table 1. Structural parameters obtained from XRD and XPS analyses [12]

HAB (mm)	d_{002} (Å)	L_a (Å)	sp^2/sp^3 ratio	π–π (%)
10	3.679	22.50	1.58	4.88
20	3.667	24.72	1.69	6.28
30	3.639	27.57	2.01	7.85
40	3.617	29.07	2.11	9.86
50	3.612	31.22	2.63	10.68
60	3.608	32.76	2.98	11.35

3.1.2. Work function

Figure 8 shows the work function of bulk soot particles as functions of the HAB. The

work function increase from 3.46 to 3.88 eV over the HAB range from 10 to 60 mm, indicating that, as soot samples gradually age, the electrons in the soot particles are more difficult to move in the interior of soot particles. The increase in work function is also related to the changes of soot structure. With the increase in HAB, the aged soot particles exhibit fewer defect sites corresponding to a less number of localized electrons existed [33] and have a greater amount of the π–π stack, as manifested in Table 1. As a result, the number of delocalized electrons is increased, which improves the depth of the attractive potential in the soot particles [11,34] and thus results in the soot particles with a larger work function. This assertion is supported by the fact that the HOPG with more π–π overlap of the electron wavefunctions and a greater number of delocalized electrons in graphite crystals has a greater value of work function (4.65 eV) [35]. Palermo et al. [27] investigated the work function for the layer architectures in the nanographene, and pointed out that more delocalized electrons in the layered architecture contribute to an increase in work function.

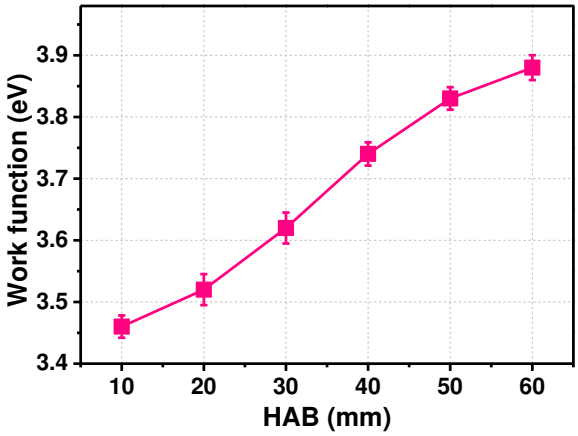

Fig. 8. Work function as functions of HABs.

It is worthy to mention that some carbon materials contain a small number of contaminants like metallic species, which can affect the electrical properties of the carbon materials. For example, if metal elements are present in the fuel during combustion, the generated soot

particles will contain these metal species. In addition, the devices used for combustion and sample collection likely result in soot particles to contain some metal species. In the present study, the *n*-heptane with HPLC grade was used to avoid containing other substances in the soot samples. No metallic species were detected in soot samples in the XPS analysis, as shown in Fig. 9. In addition, no ash content was found for soot particles after TGA oxidation. These results indicate that there are no metallic species in soot samples.

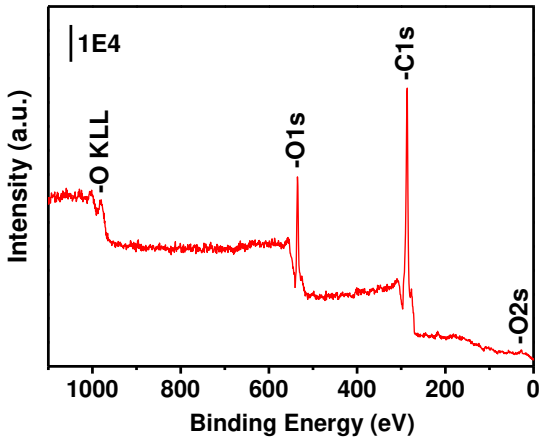

Fig. 9. XPS survey spectra of soot sample.

3.2. Soot reactivity

3.2.1. Characteristic oxidation temperature

The characteristic oxidation temperatures, including the peak temperature (T_p) and the burnout temperature (T_b), were used to evaluate the soot reactivity. T_p refers to the temperature where the maximum rate of weight loss reaches, and a higher T_p suggests harder ignition. T_b refers to the temperature where the soot oxidation is complete. Thus, the larger values of T_p and T_b indicate lower oxidation reactivity. The T_p and T_b were obtained from TGA-differential thermogravimetry (DTG) curves [36,37], as shown in Fig. 10. The obtained values for all soot samples are exhibited in Fig. 11. The values of T_p and T_b increase approximately by 28 °C and

37 °C when increasing HAB from 10 to 60 mm. These results indicate that the aged soot particles are more resistant to be ignited and burnt out. The primary reason for this behavior is that the soot particles undergo a gradual transformation into a more ordered structure when increasing the HAB, which reduces the number of available active sites and thus results in soot to be more resistant to oxidation [12,38].

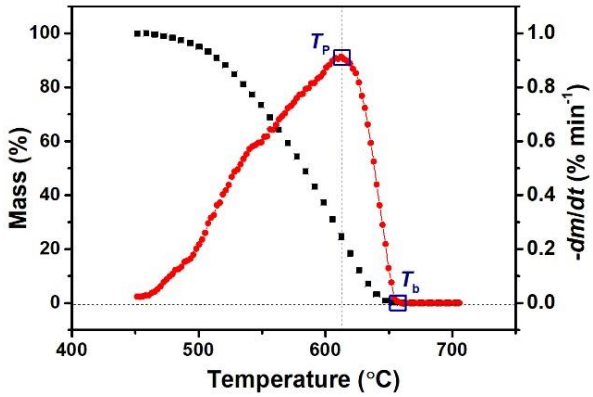

Fig. 10. Typical TGA-DTG plots for the soot particles

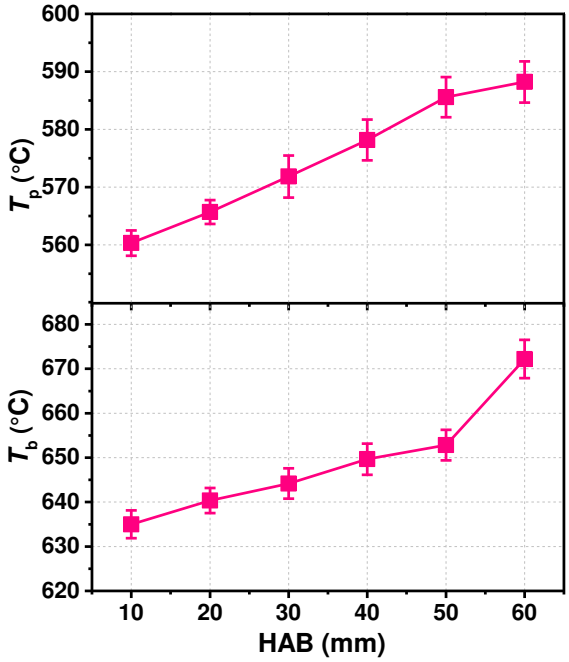

Fig. 11. Peak temperature (T_p) and burnout temperature (T_b) as functions of HABs.

3.2.2. Activation energy

299 The activation energy (E_a) was also used to assess the oxidative reactivity of soot particles
300 and to validate the results of characteristic oxidation temperature. The calculation of E_a is based
301 on the Arrhenius equation:

302 $$-\frac{dm}{dt} = k \cdot m^n = Ae^{-\frac{Ea}{RT}} m^n \quad (3)$$

303 where *m, t, k, T* and *A* are the real-time sample mass that is undergoing reaction, the reaction
304 time, the reaction rate constant, the absolute temperature of the sample and the frequency factor,
305 respectively. The *n* is the reaction order, and Al-Qurashi [39] suggested that the mean value of
306 reaction order for diesel soot particles was 0.97 $\pm$ 0.015 at various heating rates. In the study
307 of Jaramillo et al. [40], the calculated values of reaction order were 0.90 ± 0.028 for the m-
308 xylene/dodecane soot particles and 0.92 ± 0.09 for a commercial carbon black named carboxen.
309 Given the uncertainty in the values of reaction order, the assumption of reaction order equal to
310 1 (n = 1) was made in this study. In addition, the assumption of n = 1 was widely used in the
311 TGA for soot particles [15,36,41].

312 E_a and A were calculated from the slope and intercept of the plot of $\ln(-\frac{dm}{dt}\frac{1}{m})$ vs. $1/T$
313 and are listed in Table 2. As seen, the activation energy increases when increasing the HAB,
314 while the pre-exponential factor shows an opposite trend, suggesting a decline of soot reactivity.
315 Similar results were reported in the previous literatures [40,42], where the soot generated from
316 different flames also showed a decrease in pre-exponential factor with the increased activation
317 energy. On the contrary, Song et al. [43] and Zhang et al. [36] studied the reactivity of the soot
318 generated from the diesel engines, and found that the high activation energy corresponded to
319 the large pre-exponential factor.

320

Table 2. Mean activation energy (E_a) and pre-exponential factors (A) for the soot samples

HAB (mm)	Soot samples	
	E_a (kJ mol^{-1})	A (s^{-1})
10	123.37 ± 2.39	5.27×10^9
20	131.75 ± 2.98	2.96×10^8
30	140.74 ± 2.40	2.03×10^8
40	150.63 ± 2.03	5.67×10^7
50	164.44 ± 1.94	9.27×10^6
60	170.16 ± 2.69	5.68×10^6

3.3. Correlation between soot reactivity and electrical properties

3.3.1. Soot reactivity and electrical conductivity

To establish a possible correlation between soot reactivity and electrical conductivity, the T_p and E_a values for the soot samples are plotted against the logarithm of electrical conductivity (log $\overline{\sigma}$), as shown in Fig. 12. The linear degree is evaluated using the square of a linear correlation coefficient, R^2, which is calculated using the simple linear regression. It is evident that the T_p and E_a increase with the increase in log $\overline{\sigma}$, and the R^2 value is 0.93 for T_p and log $\overline{\sigma}$ and is 0.90 for E_a and log $\overline{\sigma}$. These results demonstrate that there are close positive correlations between the T_p and log $\overline{\sigma}$ as well as between the E_a and log $\overline{\sigma}$ for the soot samples. In other words, the soot reactivity has a significantly negative relationship with the log $\overline{\sigma}$. Grob et al. [13] explored the relationship between the electrical conductivity and oxidation reactivity for various carbonaceous particles using a temperature-programmed oxidation method. They revealed that the electrical conductivity showed an exponential rise with the decrease in oxidation reactivity.

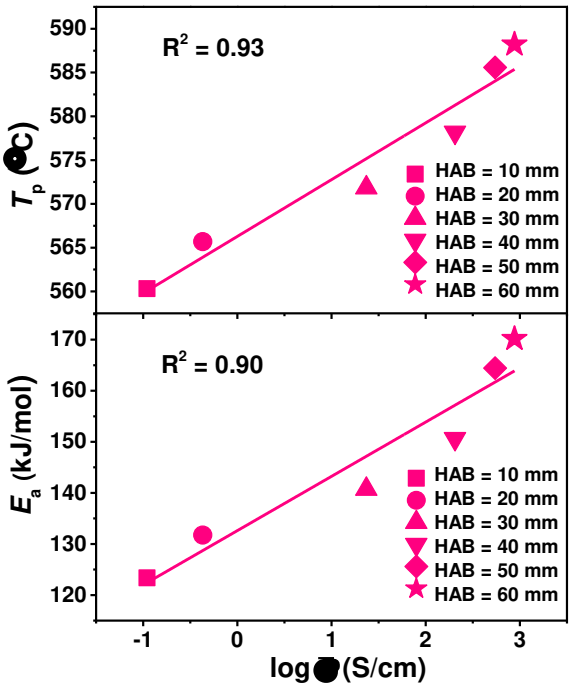

Fig. 12. Peak temperature (T_p) and activation energy (E_a) versus the logarithm of electrical conductivity.

The soot particles formed in this flame are composed of C, H and O atoms, and O and H mainly exist on soot surfaces in the form of functional groups [44,45]. To shed light on the effects of functional groups on soot reactivity and electrical conductivity, XPS analysis was used to determine the concentrations of functional groups, including hydroxyl (C-OH) and carbonyl (C=O) group. The concentrations of C-OH and C=O groups against E_a and log $\overline{\sigma}$ are plotted in Fig. 13. It is seen that the C-OH and C=O contents present marginal correlations with either the E_a or log $\overline{\sigma}$ since all the R^2 values are less than 0.36. In addition, the extent of correlations between soot nanostructure (L_a and d_{002}) and the E_a as well as log $\overline{\sigma}$ was evaluated, as shown in Fig. 14. Compared with the oxygen functional groups, the L_a and d_{002} are more important factors affecting its reactivity and electrical conductivity because all the R^2 values are above 0.90. In the study of Yehliu et al. [19,46], the soot nanostructure and reactivity showed an excellent correlation, while no relation was found between the surface oxygen

content and the soot reactivity. Seong [47] found that the considerable changes of the oxygen functional groups caused no change in soot reactivity. Lapuerta et al. [48] made a comprehensive summation about the effect of oxygenated compounds on soot reactivity published in the literatures and revealed that there is still controversy concerning the role of oxygenated compounds in reactivity. Vander Wal et al. [49] concluded that the soot reactivity was highly dependent upon its nanostructure.

An increase in the L_a and a reduction of the d_{002} will increase electrical conductivity [12,50]. On the other hand, the larger L_a and smaller d_{002} mean relatively fewer edge site carbon atoms and more carbon atoms in the basal planes. The carbon atoms in the basal planes are 100-1000 times less reactive than those at the edge sites [51], and thus more resistant to oxygen attack. The decrease in the d_{002} strengthens the binding energy of the graphene layers, and thereby these layers are more stable and more resistant to oxidation [17]. Thus, the soot particles with large L_a and small d_{002} have lower oxidative reactivity and higher electrical conductivity.

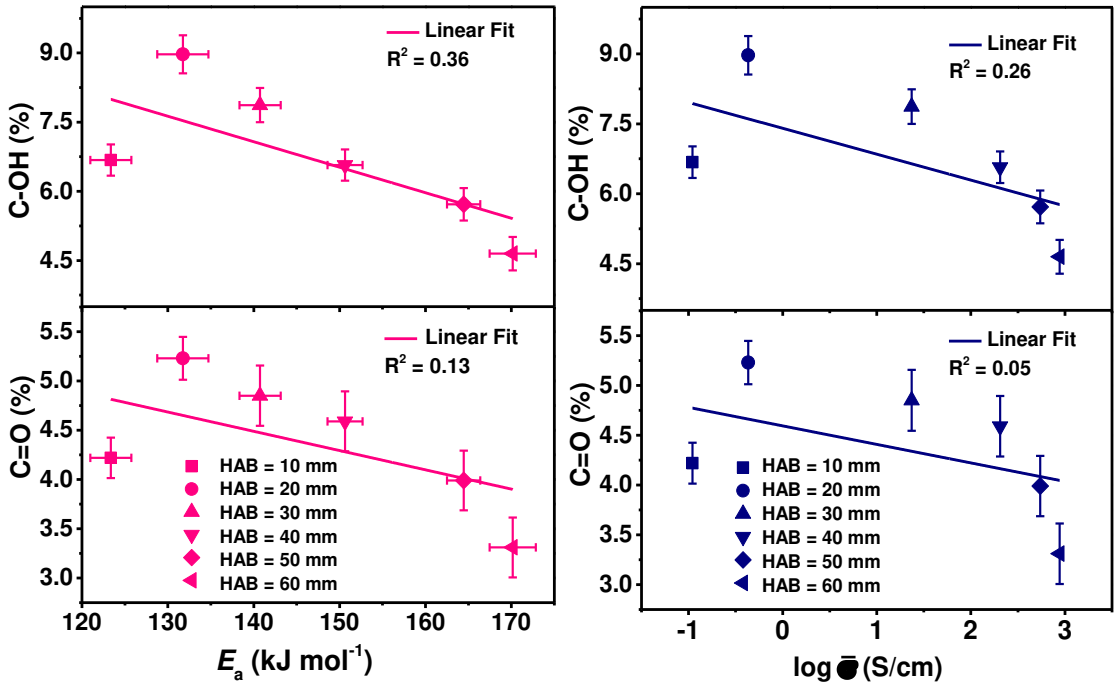

366

367 Fig. 13. Concentrations of C-OH and C=O groups as functions of E_a and log $\bar{\sigma}$.

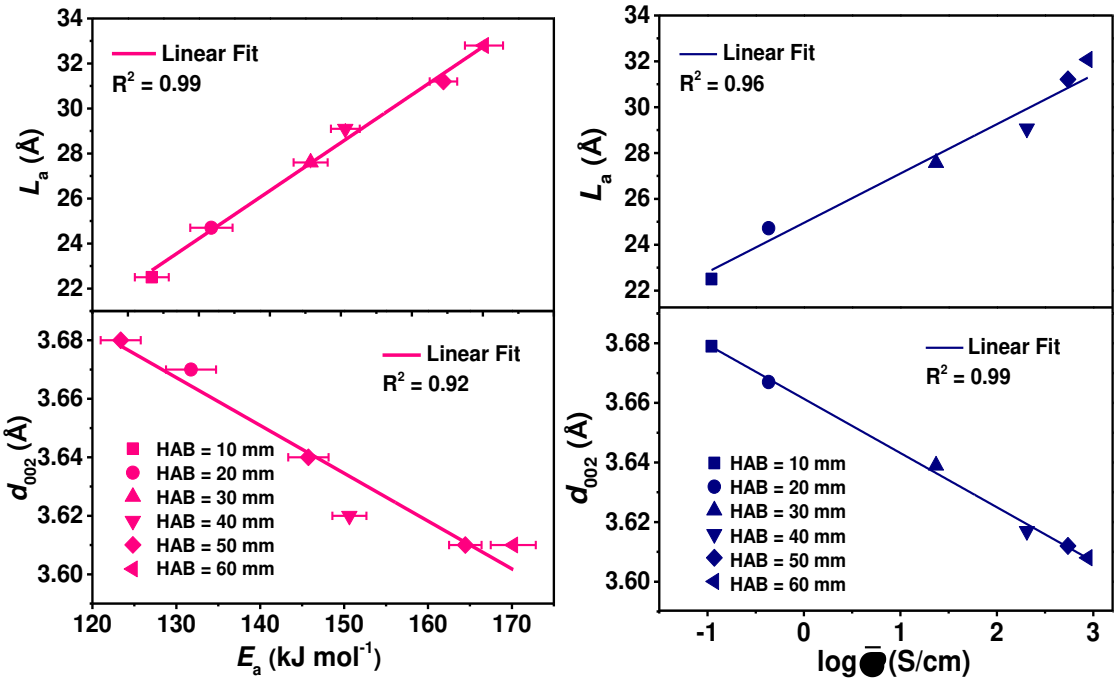

368

369 Fig. 14. L_a and d_{002} as functions of E_a and log $\bar{\sigma}$.

370 *3.3.2. Soot reactivity and work function*

371 The T_p and E_a for the soot samples against the work function are shown in Fig. 15. As seen,

372 there are clearly positive correlations between the T_p and work function as well as between E_a

373 and work function, and very high linearity (R^2=0.99) was obtained between T_p or E_a and work

function. Such results indicate that the soot reactivity has a strong negative correlation with the work function. An increase in work function corresponds to a rise in π bonding and a reduction in σ bonding in soot structure, or in other words, there are a large number of aromatic hydrocarbons (sp^2 hybridized carbon) and a low quantity of acyclic or cyclic aliphatics (sp^3 hybridized carbon) inside soot particles, as manifested in Table 1. The sp^2 hybridized carbon atoms have stronger electron resonance stabilization [17,19,38] and are more resistant to oxidation than the sp^3 hybridized carbon atoms. Consequently, the soot particles with larger work function have lower reactivity.

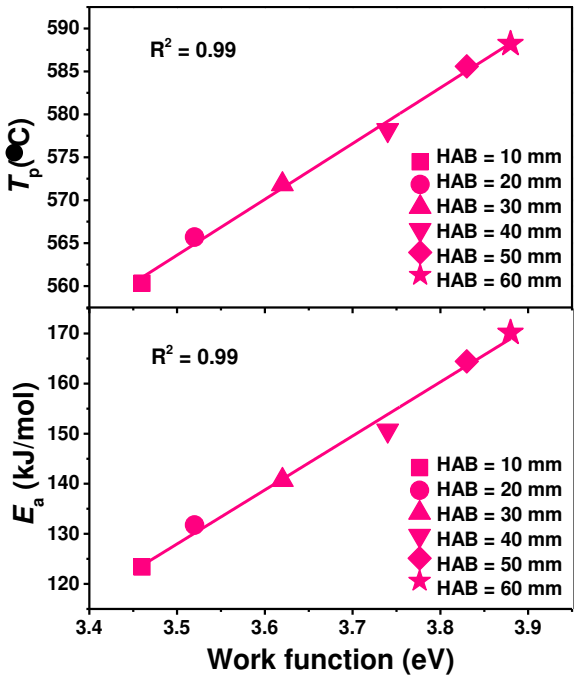

Fig. 15. Peak temperature (T_p) and activation energy (E_a) versus the work function.

In addition, it is worthy to mention that the R^2 value for soot reactivity and work function is slightly larger than that for soot reactivity and log $\overline{\sigma}$. This phenomenon is likely due to the fact that the reactivity and work function all reflect the bulk properties of soot particles, while the electrical conductivity reveals the individual particle feature without considering the interaction of soot particles.

4. Conclusion

The relationship between the oxidative reactivity and electrical properties of soot particles was studied in this study. With soot maturation, the electrical conductivity exhibits different distributions and the mean electrical conductivity increases sharply. The work function increases when soot particles gradually age. The increased work function indicates an increase in the binding of electrons in the soot particles, and thus it becomes difficult for the electrons to move in the interior of soot particles. The reactivity of soot particles reduces with the gradual maturity of soot particles. The soot reactivity exhibits a clearly negative relationship with the work function and with the logarithm of the electrical conductivity. However, the work function is more suitable to become an indicator of soot reactivity than the logarithm of electrical conductivity since it has relatively higher linearity with the reactivity.

Acknowledgments

This research was supported by the National Natural Science Foundation of China (No. 91741127 and 51921004), the Program of Tianjin Science and Technology Plan (18PTZWHZ00170), and the EU-funded projects MODALES (grant agreement No. 815189).

References

[1] G. Hagen, A. Müller, M. Feulner, A. Schott, C. Zöllner, D. Brüggemann, R. Moos, Determination of the Soot Mass by Conductometric Soot Sensors, Procedia Engineering 87 (2014) 244-247.

[2] P. Fragkiadoulakis, S. Geivanidis, Z. Samaras, Modeling a resistive soot sensor by particle deposition mechanisms, Journal of Aerosol Science 123 (2018) 76-90.

[3] T. Kamimoto, A review of soot sensors considered for on-board diagnostics application, International Journal of Engine Research 18 (2017) 631-641.

[4] M.E. Spahr, D. Goers, A. Leone, S. Stallone, E. Grivei, Development of carbon conductive additives for advanced lithium ion batteries, Journal of Power Sources 196 (2011) 3404-3413.

[5] C.A. Frysz, X. Shui, D.D.L. Chung, Use of carbon filaments in place of carbon black as the current collector of a lithium cell with a thionyl chloride bromine chloride catholyte, Journal of Power Sources (1996) 55-66.

[6] B. Marinho, M. Ghislandi, E. Tkalya, C.E. Koning, G. de With, Electrical conductivity of compacts of

graphene, multi-wall carbon nanotubes, carbon black, and graphite powder, Powder Technology 221 (2012) 351-358.
[7] D. Chen, L. Tang, J. Li, Graphene-based materials in electrochemistry, Chem Soc Rev 39 (2010) 3157-3180.
[8] M. Shiraishi, M. Ata, Work function of carbon nanotubes, Carbon, (2001) 1913–1917.
[9] Z. Yu, W. Feng, W. Lu, B. Li, H. Yao, K. Zeng, J. Ouyang, MXenes with tunable work functions and their application as electron-and hole-transport materials in non-fullerene organic solar cells, Journal of Materials Chemistry A 7 (2019) 11160-11169.
[10] H. Ago, T. Kugler, F. Cacialli, W.R. Salaneck, M.S. Shaffer, A.H. Windle, R.H. Friend, Work functions and surface functional groups of multiwall carbon nanotubes, The Journal of Physical Chemistry B 103 (1999) 8116-8121.
[11] V. Palermo, M. Palma, P. Samorì, Electronic Characterization of Organic Thin Films by Kelvin Probe Force Microscopy, Advanced Materials 18 (2006) 145-164.
[12] Y. Liu, C. Song, G. Lv, C. Fan, X. Zhang, Y. Qiao, Relationships between the electrical properties and nanostructure of soot particles in a laminar inverse diffusion flame, Proceedings of the Combustion Institute 37 (2019) 1185-1192.
[13] B. Grob, J. Schmid, N.P. Ivleva, R. Niessner, Conductivity for soot sensing: possibilities and limitations, Analytical Chemistry 84 (2012) 3586-3592.
[14] G. De Falco, M. Commodo, C. Bonavolontà, G.P. Pepe, P. Minutolo, A. D'Anna, Optical and electrical characterization of carbon nanoparticles produced in laminar premixed flames, Combustion and Flame 161 (2014) 3201-3210.
[15] J.R. Agudelo, A. Álvarez, O. Armas, Impact of crude vegetable oils on the oxidation reactivity and nanostructure of diesel particulate matter, Combustion and Flame 161 (2014) 2904-2915.
[16] G.D.J. Guerrero Peña, M.M. Alrefaai, S.Y. Yang, A. Raj, J.L. Brito, S. Stephen, T. Anjana, V. Pillai, A. Al Shoaibi, S.H. Chung, Effects of methyl group on aromatic hydrocarbons on the nanostructures and oxidative reactivity of combustion-generated soot, Combustion and Flame 172 (2016) 1-12.
[17] J. Wei, C. Song, G. Lv, J. Song, L. Wang, H. Pang, A comparative study of the physical properties of in-cylinder soot generated from the combustion of n -heptane and toluene/ n -heptane in a diesel engine, Proceedings of the Combustion Institute 35 (2015) 1939-1946.
[18] I.C. Jaramillo, C.K. Gaddam, R.L. Vander Wal, J.S. Lighty, Effect of nanostructure, oxidative pressure and extent of oxidation on model carbon reactivity, Combustion and Flame 162 (2015) 1848-1856.
[19] K. Yehliu, R.L. Vander Wal, O. Armas, A.L. Boehman, Impact of fuel formulation on the nanostructure and reactivity of diesel soot, Combustion and Flame 159 (2012) 3597-3606.
[20] M. Schejbal, M. Marek, M. Kubíček, P. Kočí, Modelling of diesel filters for particulates removal, Chemical Engineering Journal 154 (2009) 219-230.
[21] M. Schejbal, P. Kočí, M. Marek, M. Kubíček, Modelling of wall-flow filters for diesel particulate removal, Computer Aided Chemical Engineering, Elsevier2009, pp. 803-808.
[22] P. Chen, J. Wang, Air-fraction modeling for simultaneous diesel engine NOx and PM emissions control during active DPF regenerations, Applied Energy 122 (2014) 310-320.
[23] B. Zhao, Z. Yang, J. Wang, M.V. Johnston, H. Wang, Analysis of Soot Nanoparticles in a Laminar Premixed Ethylene Flame by Scanning Mobility Particle Sizer, Aerosol Science and Technology 37 (2003) 611-620.
[24] W. Rivera, J. Perez, R. Ruoff, D. Lorents, R. Malhotra, S. Lim, Y. Rho, E. Jacobs, R. Pinizzotto, Scanning tunneling microscopy current–voltage characteristics of carbon nanotubes, Journal of Vacuum Science & Technology B: Microelectronics and Nanometer Structures Processing, Measurement, and Phenomena 13 (1995) 327-330.

460 [25] G. Zajac, J. Gallas, A. Alvarado‐Swaisgood, Tunneling microscopy verification of an x‐ray scattering‐
461 derived molecular model of tyrosine‐based melanin, Journal of Vacuum Science & Technology B:
462 Microelectronics and Nanometer Structures 12 (1994) 1512-1516.
463 [26] A.C. Barone, A. D'Alessio, A. D'Anna, Morphological characterization of the early process of soot formation
464 by atomic force microscopy, Combustion and Flame 132 (2003) 181-187.
465 [27] V. Palermo, M. Palma, Ž. Tomović, M.D. Watson, R. Friedlein, K. Müllen, P. Samorì, Influence of Molecular
466 Order on the Local Work Function of Nanographene Architectures: A Kelvin‐Probe Force Microscopy Study,
467 ChemPhysChem 6 (2005) 2371-2375.
468 [28] D.S. McLachlan, M.B. Heaney, Complex ac conductivity of a carbon black composite as a function of
469 frequency, composition, and temperature, Physical Review B 60 (1999) 12746-12751.
470 [29] A.K. Kercher, D.C. Nagle, AC electrical measurements support microstructure model for carbonization: a
471 comment on 'Dielectric relaxation due to interfacial polarization for heat-treated wood', Carbon 42 (2004) 219-
472 221.
473 [30] C.K. Gaddam, R.L. Vander Wal, Physical and chemical characterization of SIDI engine particulates,
474 Combustion and Flame 160 (2013) 2517-2528.
475 [31] Z. Su, W. Zhou, Y. Zhang, New insight into the soot nanoparticles in a candle flame, Chemical
476 Communications 47 (2011) 4700-4702.
477 [32] Z.R. Yue, W. Jiang, L. Wang, S.D. Gardner, C.U. Pittman, Surface characterization of electrochemically
478 oxidized carbon fibers, Carbon 37 (1999) 1785-1796.
479 [33] P. Stallinga, Electronic transport in organic materials: Comparison of band theory with percolation/(variable
480 range) hopping theory, Advanced Materials 23 (2011) 3356-3362.
481 [34] R. Friedlein, X. Crispin, C.D. Simpson, M.D. Watson, F. Jäckel, W. Osikowicz, S. Marciniak, M.P. de Jong,
482 P. Samorí, S.K.M. Jönsson, M. Fahlman, K. Müllen, J.P. Rabe, W.R. Salaneck, Electronic structure of highly
483 ordered films of self-assembled graphitic nanocolumns, Physical Review B 68 (2003) 195414.
484 [35] C. Sommerhalter, T.W. Matthes, T. Glatzel, A. Jäger-Waldau, M.C. Lux-Steiner, High-sensitivity quantitative
485 Kelvin probe microscopy by noncontact ultra-high-vacuum atomic force microscopy, Applied Physics Letters
486 75 (1999) 286-288.
487 [36] D. Zhang, Y. Ma, M. Zhu, Nanostructure and oxidative properties of soot from a compression ignition engine:
488 The effect of a homogeneous combustion catalyst, Proceedings of the Combustion Institute 34 (2013) 1869-1876.
489 [37] S.Y. Yorulmaz, A.T. Atimtay, Investigation of combustion kinetics of treated and untreated waste wood
490 samples with thermogravimetric analysis, Fuel Processing Technology 90 (2009) 939-946.
491 [38] Z. Li, C. Song, J. Song, G. Lv, S. Dong, Z. Zhao, Evolution of the nanostructure, fractal dimension and size
492 of in-cylinder soot during diesel combustion process, Combustion and Flame 158 (2011) 1624-1630.
493 [39] The impact of carbon dioxide and exhaust gas recireculation on the oxidative reactivity of soot from ethylene
494 flames and diesel engines, The Pennsylvania State University, (2007).
495 [40] I.C. Jaramillo, C.K. Gaddam, R.L. Vander Wal, C.-H. Huang, J.D. Levinthal, J.S. Lighty, Soot oxidation
496 kinetics under pressurized conditions, Combustion and Flame 161 (2014) 2951-2965.
497 [41] G.A. Stratakis, A.M. Stamatelos, Thermogravimetric analysis of soot emitted by a modern diesel engine run
498 on catalyst-doped fuel, Combustion and Flame 132 (2003) 157–169.
499 [42] Y. Zhang, Low temperature oxidation of biodiesel surrogates in a motored engine and the oxidation behavior
500 of soot generated from the combustion of a biodiesel surrogate in a diffusion flame, The Pennsylvania State
501 University, Ph.D. thesis, (2010).
502 [43] J. Song, M. Alam, A.L. Boehman, Impact of alternative fuels on soot properties and DPF regeneration,
503 Combustion Science and Technology 179 (2007) 1991-2037.

[44] J.P. Cain, P.L. Gassman, H. Wang, A. Laskin, Micro-FTIR study of soot chemical composition—evidence of aliphatic hydrocarbons on nascent soot surfaces, Physical Chemistry Chemical Physics 12 (2010) 5206.
[45] J.P. Cain, J. Camacho, D.J. Phares, H. Wang, A. Laskin, Evidence of aliphatics in nascent soot particles in premixed ethylene flames, Proceedings of the Combustion Institute 33 (2011) 533-540.
[46] K. Yehliu, Impacts of fuel formulation and engine operating parameters on the nanostructrue and reactivity of diesel soot, The Pennsylvania State University, Ph.D. thesis, (2010).
[47] H.J. Seong, Impact of oxygen enrichment on soot properties and soot oxidative reactivity, The Pennsylvania State University, Ph.D. thesis, (2010).
[48] M. Lapuerta, J. Rodríguez–Fernández, J. Sánchez-Valdepeñas, Soot reactivity analysis and implications on diesel filter regeneration, Progress in Energy and Combustion Science 78 (2020).
[49] R.L. Vander Wal, V.M. Bryg, M.D. Hays, Fingerprinting soot (towards source identification): Physical structure and chemical composition, Journal of Aerosol Science 41 (2010) 108-117.
[50] Y.-R. Rhim, D. Zhang, D.H. Fairbrother, K.A. Wepasnick, K.J. Livi, R.J. Bodnar, D.C. Nagle, Changes in electrical and microstructural properties of microcrystalline cellulose as function of carbonization temperature, Carbon 48 (2010) 1012-1024.
[51] H. Marsh, K. Kuo, Kinetics and catalysis of carbon gasification, Introduction to carbon science, Elsevier1989, pp. 107-151.